npj | 2D Materials and Applications

www.nature.com/npj2dmaterials

ARTICLE OPEN

An atom-to-circuit modeling approach to all-2D metal–insulator–semiconductor field-effect transistors

Biswapriyo Das[1] and Santanu Mahapatra[1]

Vertical stacking of heterogeneous two-dimensional (2D) materials has received considerable attention for nanoelectronic applications. In the semiconductor industry, however, the process of integration for any new material is expensive and complex. Thus, first principles-based models that enable systematic performance evaluation of emerging 2D materials at device and circuit level are in great demand. Here, we propose an 'atom-to-circuit' modeling framework for all-2D MISFET (metal–insulator–semiconductor field-effect transistor), which has recently been conceived by vertically stacking semiconducting transition metal dichalcogenide (e.g., MoS_2), insulating hexagonal boron nitride and semi-metallic graphene. In a multi-scale modeling approach, we start with the development of a first principles-based atomistic model to study fundamental electronic properties and charge transfer at the atomic level. The energy band-structure obtained is then used to develop a physics-based compact device model to assess transistor characteristics. Finally, the models are implemented in a circuit simulator to facilitate design and simulation of integrated circuits. Since the proposed modeling framework translates atomic level phenomena (e.g., band-gap opening in graphene or introduction of semiconductor doping) to a circuit performance metric (e.g., frequency of a ring oscillator), it may provide solutions for the application and optimization of new materials.

npj 2D Materials and Applications (2018)2:28 ; doi:10.1038/s41699-018-0073-3

INTRODUCTION

Functionality of an electronic device originates from the interfacial properties of its constituent materials. Advancement of nanofabrication technology has opened up the possibility of realizing interfaces at their 'ultimate-limit' by vertical stacking[1–3] or parallel stitching[4] of 2D materials. Since these new materials inherit diverse electronic and opto-electronic properties, novel device functionalities could be engineered from such atomically thin interfaces.[5] In such vertically stacked van der Waal's heterostructures (vdWH),[6] the individual layers are 'glued' together by weak van der Waal's (vdW) forces of interaction,[7] whereas the in-plane atoms are strongly bound by covalent or ionic bonds. The hetero-interfaces thus produced, are atomically sharp and self-passivated, i.e., free of dangling bonds and trapped charges. These subtle attributes have encouraged the application of vdWHs as a platform for constructing sophisticated nano-devices such as field-effect transistors (FETs),[8–10] tunnel devices,[11,12] photo-detector,[13] light-emitting diode,[14,15] solar cell,[16] flexible electronics[10] etc.

Among all types of FET devices studied theoretically or fabricated for experimental and commercial purposes, the MIS (metal–insulator–semiconductor) structure, which substitutes metal (or highly doped polysilicon) by semi-metallic graphene, SiO_2 (or high-K gate dielectric) by insulating h-BN, and Si by MoS_2, could pave the way for realizing thinnest possible FET. Roy et al.[9] have demonstrated such experimental device that exhibits n-type behavior with an ON/OFF current ratio $>10^6$ and ~33 cm^2/Vs electron mobility. The work of Lee et al.[10] evidences implementation of a flexible and transparent FET claiming field-effect mobilities up to 45 cm^2/Vs. At the same time, Jeong et al.[12] have demonstrated the operation of a MIS diode, where carrier tunneling is the principle transport process. In a similar device Vu et al.[17] have obtained high photocurrent/dark-current ratio $>10^5$ and ultrahigh photodetectivity of 2.6×10^{13} Jones. Using first principles-based analysis, Zan et al.[18] have demonstrated the enhancement of interlayer coupling and linear charge transfer between graphene and MoS_2 layers upon application of homogeneous electric field, and conversely the weakening of interlayer coupling under applied biaxial strain.

It should, however, be noted that introduction of any new material in the process integration phase of technology development in semiconductor industry is an expensive and time-consuming affair. It is also a difficult task to select appropriate 2D materials from the plethora[19] without assessing their performance at circuit level. Thus, a modeling framework, that enables systematic performance evaluation of new materials at device and circuit levels before entering into capital-intensive manufacturing phase, is in great demand. Such models must be first principles based so that the assessment could be conducted even before the wafer is available. Despite significant efforts on synthesis and fabrication, community lacks such modeling framework, which can predict integrated circuit performance solely from the crystallographic information of the constituent transistor materials.

In this article, we propose hierarchical bottom-up modeling methodology for all-2D MISFET that bridges between three levels of abstraction viz. material, device, and circuit. It is noteworthy that unlike conventional MOSFETs (Metal Oxide Semiconductor Field Effect Transistors), in this device, the gate electrostatics is dictated by the effects of dipole–dipole interactions,[20–22] prevailing at the interfaces of a typical vdWH. Thus, modeling

[1]Department of Electronic Systems Engineering, Nano-Scale Device Research Laboratory, Indian Institute of Science (IISc) Bangalore, Bangalore 560012, India
Correspondence: Biswapriyo Das (biswapriyodas1@gmail.com)

Received: 10 April 2018 Revised: 5 July 2018 Accepted: 13 July 2018
Published online: 06 August 2018

methodologies reported earlier for 2D-semiconductor FETs[23–25] are not applicable here. Apart from this, the band-gap opening in graphene due to vdW interactions poses additional complexity to the device physics. To capture all these intricate atomic level phenomena at circuit level, we adopt several sophisticated techniques, e.g., density functional theory (DFT)-based atomistic model, tight-binding Hamiltonian for graphene encompassing the effect of sublattice symmetry breaking, Fermi-Dirac (FD) distribution of mobile charge carriers, drift-diffusion (DD) formalism[26] with bias-dependent diffusivity, and piecewise charge linearization (PWCL) technique.[27] Finally, we arrive at the closed-form expressions for drain current and terminal charges for the all-2D MISFET, which are implemented in professional circuit simulator using Verilog-AMS interface in order to conduct static and transient simulation of integrated circuits. We induce bandgap variation in graphene by tuning the interlayer distance between hBN and graphene[28], and observe its effect at transistor and circuit level. Since doped MoS_2 is now commercially available,[29] we further demonstrate a material-device-circuit co-assessment scheme based on the semiconductor doping. The Verilog-AMS module developed in this work connects the material modeling tools[30–32] with industrial electronic design automation tools[33,34] and thus promises to provide a solution to the DTCO (design-technology co-optimization) challenges for new materials.

RESULTS

The proposed 'atom-to-circuit' modeling framework has been synopsized in Fig. 1. We start with the DFT-based atomistic model development of vdWH in order to probe the energy band structure and interlayer charge transfer. Dielectric constant values and carrier mobilities of the materials have been acquired from reported first principle-based calculations.[35,36] The material level attributes thus obtained are then used to develop physics-based compact device model to understand the properties of MIS capacitor and FET. Limited by the computational budget, we consider only two layers of hBN for developing the atomistic model, although experiments[12,17] were conducted using several layers of it. However, our device model parameters could easily be calibrated to any number of hBN-layer based vdWH. Finally, those closed-form expressions of current and charges are implemented in professional circuit simulator to enable design and simulation of a digital logic inverter and a 15-stage ring oscillator.

Energy band structure and interlayer charge transfer

The geometrically optimized atomic structure of graphene-hBN-hBN-MoS_2 is shown in Fig. 2(a) (see methods for details). The equilibrium spacings between graphene-hBN (d_1), MoS_2-hBN (d_2) and hBN-hBN (d_3) were found to be 3.2, 4.9 and 3.1 Å respectively. It is well-known[28,37–42] that the energy gap at Dirac point of graphene is strongly influenced by the substrates and the stacking pattern of the layers. This is due to the fact that there is always an interplay between the strain energy of graphene, when placed on a substrate[38] and the reduction of symmetry from C_{6v} to C_{3v} point group due to breaking of the chemical equivalency of carbon lattice sites.[21] For graphene on top of hBN (CB configuration), there is an effective charge transfer from C_0 (C atom on top of BN hexagon center) atom to C_B (C atom on top of B atom) atom owing to the difference in electronegativities of B and N atoms of hBN.[41] It results into an onsite energy difference of C atoms at different sublattices. Thus, sublattice symmetry is broken and the energy levels of p_z orbitals of carbon atoms shift to open a bandgap, exactly equal to the onsite energy difference at the Dirac point of otherwise gapless semi-metallic graphene. The band-gap opening in graphene (analogous to depletion in poly-silicon gate of Si MOSFETs) is expected to play a very crucial role in dictating the MIS capacitor and transistor characteristics. Since this bandgap might be perturbed due to material defects, externally applied strain or any uncertainties in process variations, we emulate such bandgap variation by changing the graphene–hBN interlayer distance d_1 (3.2 ± 0.2 Å) of the graphene-hBN-MoS_2 system.

Figure 2(b) illustrates the band structures of the vdWH with d_1 varying from 3.0 to 3.4 Å with an interval of 0.2 Å. The Fermi level (E_F) for the band structure is referenced to 0 eV. As depicted in Fig. 2(b), graphene has a bandgap of 0.06 eV at equilibrium separation and the bandgap almost doubles at 0.2 Å decrease of d_1. Besides, the energy dispersion near Dirac point of graphene resembles more of a parabolic nature[28] rather than linear one and the parabolicity increases with the reduction of d_1. It also reveals that the otherwise pristine MoS_2 becomes p-type in nature due to vdW stacking at equilibrium spacing ($d_1 = 3.2$ Å), which is in agreement with the reported hBN-MoS_2 heterostructure.[43] We further observe that the p-type nature becomes more evident with decreasing values of d_1, whereas it tends to behave like n-type semiconductor while d_1 increases from its equilibrium value. However, the bandgap of MoS_2 remains unaltered with a value of 1.71 eV. The absolute numeric values of Δ_{GC}, Δ_{GV}, Δ_{MC}, Δ_{MV}, which represent the shifts in energy of graphene-CBM (conduction band minima), graphene-VBM (valence band maxima), MoS_2-CBM and MoS_2-VBM respectively, as measured from E_F and the values of effective masses (viz. m^*_{eG}, m^*_{hG}, m^*_{eM}, m^*_{hM}; where the subscripts denote e: electron, h: hole, G: graphene, M: MoS_2) as calculated from band structures, are presented in Table 1 (m_0 being rest mass of electron).

The charge transfer from C_0 to C_B atom can be quantified by the Mulliken population analysis as listed in Table 2. It reveals the fact that the amount of charge transfer (Δ_q) increases with decreasing values of d_1, indicating wider bandgap opening in graphene. To further investigate the charge redistribution at the hetero-interfaces, we calculate the electron density difference (EDD), $\Delta\rho$, for three different values of d_1, averaged along the z direction as shown in Fig. 2(c). The EDD is computed as $\Delta\rho = \rho_{G+hBN+MoS_2} - \rho_G - \rho_{hBN} - \rho_{MoS_2}$, where ρ represents electron density. In Fig. 2(c), both charge accumulation (positive peaks) and depletion (negative peaks) regions are found at the interfaces. Clearly, the charge redistribution is more pronounced at the graphene–hBN interface rather than hBN–hBN or hBN–MoS_2 interfaces and it increases at the graphene–hBN interface with decreasing d_1, while remains almost unaltered at the other two interfaces. When $d_1 < 3.2$ Å, the surface charge repulsion (Pauli repulsion) dictates the charge redistribution in graphene–hBN interface, whereas for $d_1 > 3.2$ Å, an accumulation region at the middle of the interlayer spacing indicates strong orbital hybridization[22] between graphene and hBN. Quite obviously, there is a concoction of Pauli repulsion and orbital hybridization prevalent at $d_1 = 3.2$ Å. This orbital hybridization originates from the orbital contributions of distinct atoms to the band structure (detailed in Supplymentary Information). The VBM and CBM of graphene at K-point in Brillouin zone are contributed by the p_z orbitals (π-bonding and π^*-antibonding states respectively) of C atoms, which are prone to be perturbed by the interactions with π-electron clouds of hBN, localized around N centers. But this should not be the case for MoS_2 since its CBM and VBM are mostly composed of d_{z^2} and $d_{x^2-y^2}$ orbitals of Mo atoms; whose interactions with s and p orbitals of B and N atoms are very limited. However, a comparatively small accumulation region at MoS_2–hBN interface indicates orbital hybridization between s and p orbitals of hBN and nearer S atoms. Interestingly, there is a dipole formation at MoS_2–hBN interface which in turn causes the work-function modification,[22] signifying band alignment of MoS_2 and hBN. This effectuates a charge transfer between MoS_2 and hBN, thereby dictating the p-type character of MoS_2. To further quantify the charge redistribution, we have calculated the area under EDD curve at MoS_2–hBN (between hBN and nearest S atoms) and graphene–hBN interfaces as detailed in Table 3. The

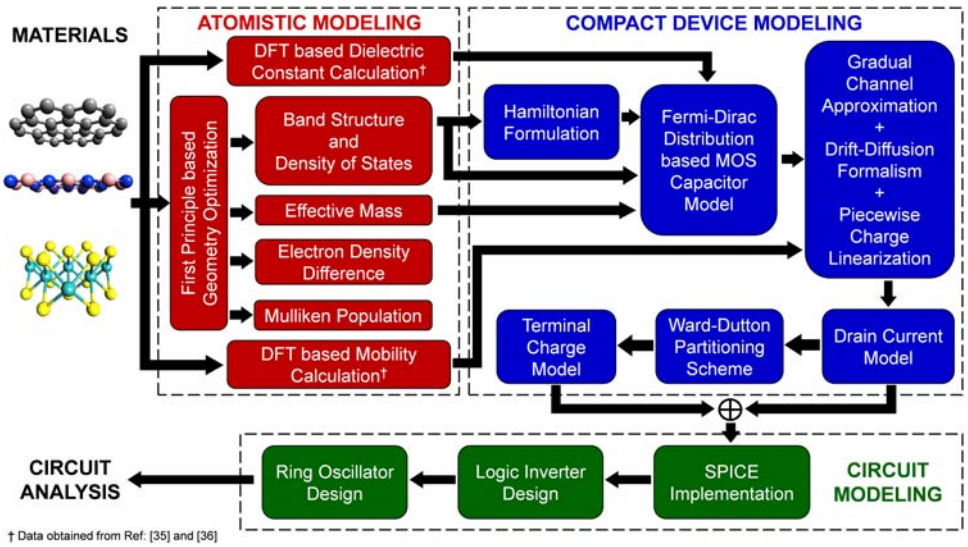

Fig. 1 Synopsis of 'atom-to-circuit' multi-scale modeling methodology. First, the band structure parameters are extracted from first principles-based atomistic calculations and the charge transfer in atomic level is analyzed. The extracted parameters are then used for developing a compact device model of the vdWH-based MISFET. Then that model is implemented in commercial circuit simulators using its Verilog–AMS interface

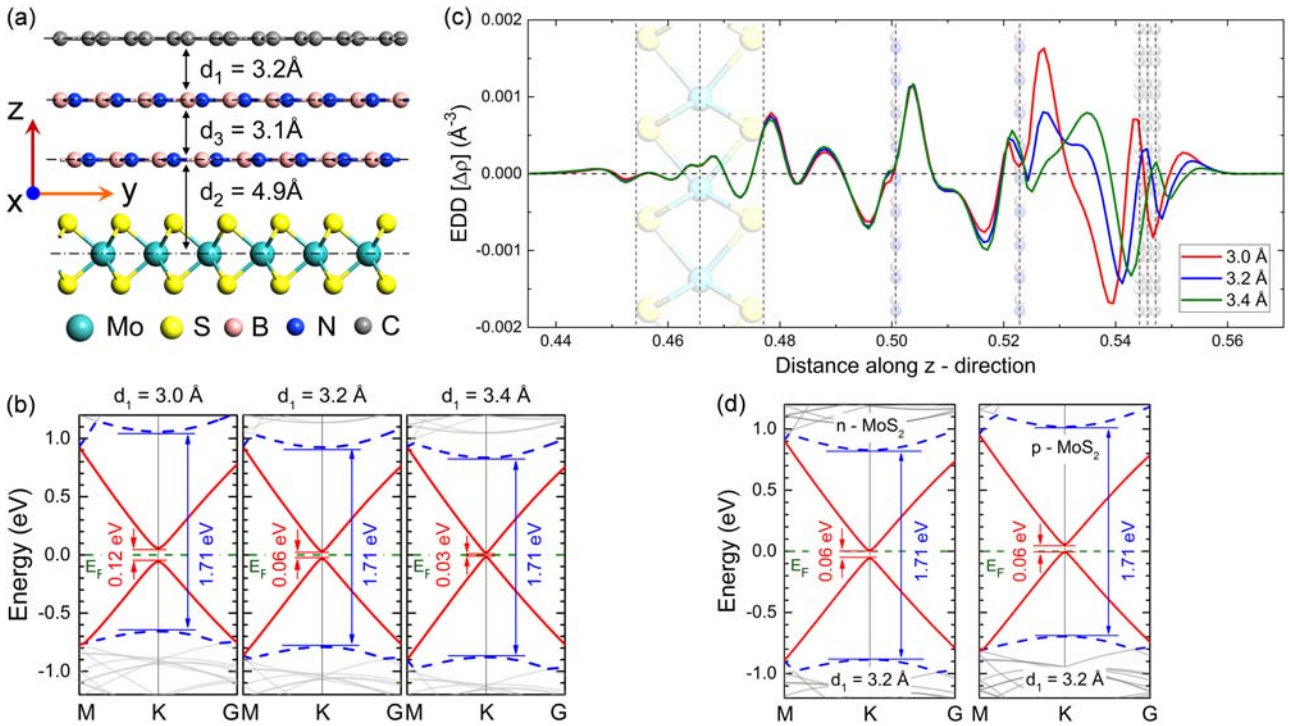

Fig. 2 **a** Atomic model for graphene-hBN-hBN-MoS_2 vdWH with the equilibrium interlayer spacings indicated. Color codes for the atoms are:- cyan: molybdenum, yellow: sulfur, pink: boron, blue: nitrogen, gray: carbon. **b** Energy band structures of the vdWH with d_1 varying from 3.0 to 3.4 Å with a stepping of 0.2 Å. Red and blue-dashed bands correspond to graphene and MoS_2 respectively. It depicts that with decreasing d_1, band gap of graphene increases and MoS_2 becomes more p-type with an unaltered band gap of 1.71 eV. **c** Electron density difference (EDD) plot of the vdWH showing greater charge redistribution in graphene–hBN interface than MoS_2–hBN interface. This charge redistribution at graphene–hBN interface increases with decreasing d_1. **d** Energy band structures of the vdWH comprising of n-type and p-type MoS_2 monolayers with a doping concentration of 1×10^{19} cm^{-3} (both n and p), indicating unaltered band gaps of both graphene and MoS_2. It shows that although graphene is kept pristine, effectively it becomes n or p-type in accordance to the type of doping due to interlayer charge transfer

higher the value, more pronounced is the charge redistribution with more chemical interactions occurring at the interface. As depicted, the comparatively smaller area under EDD at MoS_2–hBN interface remains almost unaltered with variation of d_1, while for graphene–hBN interface it increases with decreasing d_1. The threshold voltage of MIS capacitor is expected to increase with the bandgap broadening in graphene and the upward shifting of MoS_2 band structure. Furthermore, since the charge distribution at the interlayer spacing can be perceived as a way of energy storing, the increment of EDD area at the graphene–hBN interface with

Table 1. Band-structure parameters

d_1 (Å)	Δ_{GC} (eV)	Δ_{GV} (eV)	Δ_{MC} (eV)	$\Delta_{MV}(eV)$	m^*_{eG}/m_0	m^*_{hG}/m_0	m^*_{eM}/m_0	m^*_{hM}/m_0
3.0	0.059	0.059	1.058	0.657	0.017	0.017	0.56	0.632
3.2	0.032	0.032	0.923	0.791	0.009	0.009	0.56	0.632
3.4	0.018	0.018	0.835	0.879	0.005	0.005	0.56	0.632
n-3.2	0.008	0.058	0.828	0.885	0.009	0.009	0.56	0.632
p-3.2	0.057	0.008	1.018	0.696	0.009	0.009	0.56	0.632

Table 2. Mulliken population

d_1 (Å)	C_B	C_0	Δ_q
3.0	3.99752	3.98684	0.01068
3.2	3.99608	3.99392	0.00216
3.4	3.99796	3.99648	0.00148

Table 3. Area under EDD (Å^{-2})

d_1 (Å)	hBN-MoS_2 Interface ($\times10^{-5}$)	G-hBN Interface ($\times10^{-5}$)
3.0	0.71	1.77
3.2	0.72	1.19
3.4	0.72	1.18

decreasing d_1 signifies possible enhancement of the quantum capacitance of graphene as will be elucidated in the next section.

The electronic band structure of the aforesaid vdWH comprising of n-type and p-type MoS_2 monolayer is depicted in Fig. 2(d). The downward or upward shifting of the bands with respect to the Fermi level is clearly visible for n-type and p-type doping respectively; although the band gaps and effective masses of graphene and MoS_2 remain unaltered. The values of effective masses and absolute positions of conduction and valence band edges of graphene and MoS_2 (n or p-type) in the energy scale are provided in Table 1. Figure 2(d) reveals that even though the graphene layer is kept pristine and only MoS_2 layer undergoes electrostatic doping, due to interlayer charge transfer and thereby charge redistribution, graphene also becomes effectively n-type or p-type according to the doping in MoS_2. Since this is mediated by interlayer charge transfer, graphene should eventually tend to remain pristine if we increase the number of hBN layers in between graphene and MoS_2.

MIS capacitor and transistor characteristics

It is worth noting that in previous studies[18] the electric field within the material system was considered to be homogeneous. The charge distribution inside a material system under spatially varying electric field is beyond the scope of pure DFT calculations.[44] The proposed model is thus useful to understand the C-V characteristics of the vdWH system. The transistor schematic of the concerned vdWH-based MISFET is illustrated in Fig. 3(a), where 'S' and 'D' denotes source and drain (deemed to be 'ideal') respectively, V_{GS} and V_{DS} refer to gate-to-source and drain-to-source voltage respectively. The non-ideal effects arising from the charges, unintentionally present in semiconductor substrate have been neglected in this work. The coined device symbol is portrayed in inset of Fig. 3(a). The electrical equivalent circuit of this MIS capacitor is shown in Fig. 3(b) that consists of three capacitors in series connection viz. quantum capacitance of graphene (C_{qG}), insulator capacitance of bilayer hBN (C_I) and quantum capacitance of MoS_2 (C_{qM}). Considering the semiconductor body to be grounded, if we apply a gate voltage V_G in graphene, equal amount of charge will be stored in all three capacitors, thereby causing a potential drop of Ψ_G across C_{qG}, Ψ_I across C_I and Ψ_S across C_{qM}. For convenience, the relevant band structure parameters used in our model are depicted in Fig. 3(c). The calibrated tight-binding Hamiltonian (see methods section) and corresponding energy dispersion relations, used for device model development, are found to be in good agreement with DFT calculation as shown in Fig. 3(d), where $m^*_{eG} = \Delta_{GC}/v_F^2$ (v_F being the reduced Fermi velocity of graphene over hBN) and $m^*_{hG} = \Delta_{GV}/v_F^2$. For a given bias condition, the variation of the inversion charge density in MoS_2 layer (Q_I') along the MISFET channel as a function of surface potential Ψ_S is demonstrated in Fig. 3(e). Similar to conventional Si-MOSFETs, Q_I' holds a linear relationship with Ψ_S as long as the band gap opening in graphene is small. However, significant non-linearity creeps in as the bandgap broadens, which necessitates PWCL technique based drain current and terminal charge modeling as discussed in methods section.

Figure 4(a) and (b) respectively depicts the plots of C_{qG} and C_{qM} as a function of V_{GS} (swept from 0 V to 1.5 V) with V_{DS} set to 0 V. It is found that both C_{qG} and C_{qM} operate within the quantum capacitance limit (i.e., $q^2 g_{2D}$, where q is fundamental electronic charge and g_{2D} is 2D density of states). The value of C_{qG} increases as we decrease the interlayer separation due to the increased charge redistribution at graphene–hBN interface as mentioned before. However, unlike C_{qG}, C_{qM} doesn't even tend to saturate at large gate bias of 1.5 V. The total gate capacitance of the device as seen from the gate terminal, i.e. C_{gg}, can be calculated as $C_{gg} = \left(1/C_{qG} + 1/C_I + 1/C_{qM}\right)^{-1}$ using the value of C_I, computed to be ~26.5 fF considering the relative permittivity of bilayer hBN, i.e. ε to be 1.9.[35] The variation of C_{gg} as a function of V_{GS} has been plotted in Fig. 4(c) keeping $V_{DS} = 0$ V. It reveals that saturated C_{gg} increases with increasing bandgap of graphene and the crossing between individual graphs is a direct consequence of threshold voltage increment of the device. In the overall capacitance-voltage characteristics, C_{gg} is mostly dominated by C_{qG}.

Figure 4(d) and (e) respectively provides the transfer and drain characteristics of the MISFET, where I_{DC} denotes the dc drain current flowing in the channel. The transfer characteristics of Fig. 4 (d) clearly points out the threshold voltage increment of the transistor as bandgap opening in graphene becomes more pronounced with decreasing d_1. However, the subthreshold slope remains almost unaltered in all three cases. The subthreshold swings were calculated to be ~60.48 mV/decade for all cases. This is because in subthreshold regime C_{qM} is found to be much smaller than C_{qG} and C_I, which makes the subthreshold slope factor nearly unity. In the drain characteristics, delineated in Fig. 4 (e), I_{DC} attains a maximum value of ~60 μA/μm for $d_1 = 3.2$ Å. Since the threshold voltage is maximum for $d_1 = 3.0$ Å, it bears the lowest pinch-off voltage (V_P) among all three cases and that's why the corresponding drain current saturates at earliest having smallest saturation drain current value ($I_{D,sat}$). From similar analogy, the transistor with $d_1 = 3.4$ Å has highest V_P and therefore it should have maximum $I_{D,Sat}$. However, this is not the

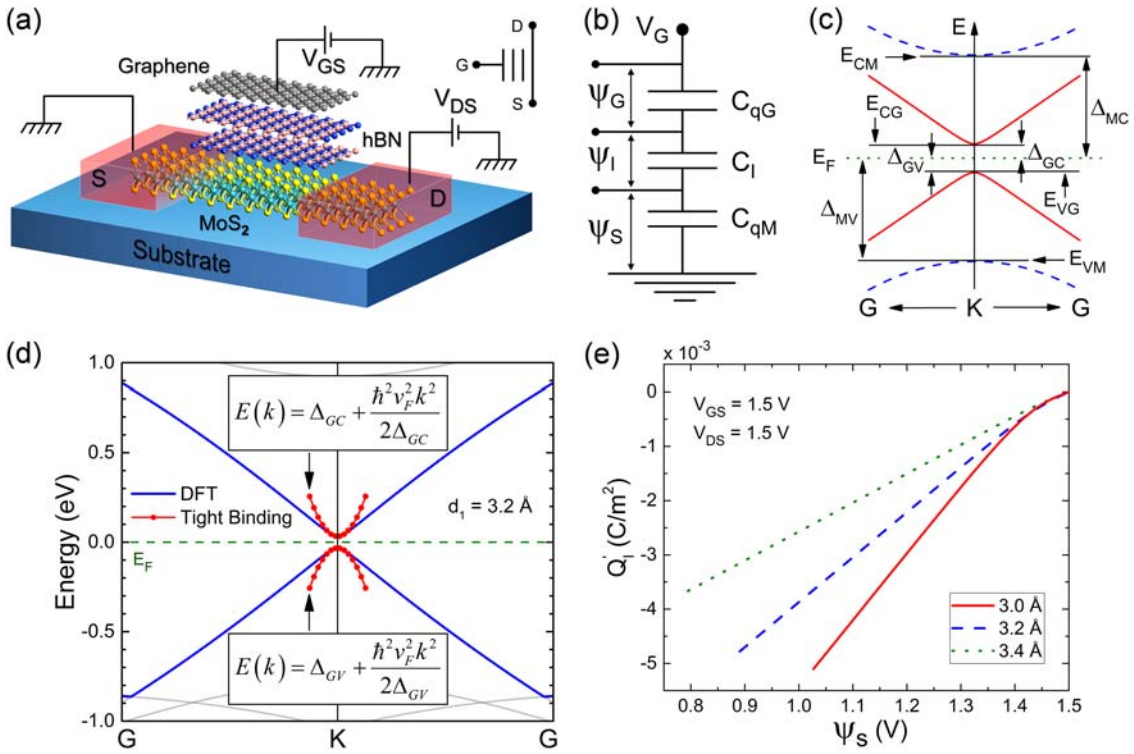

Fig. 3 **a** Schematic representation of the vdWH-based MISFET. The coined device symbol is shown in the inset. **b** Electrical equivalent circuit of the MIS capacitor comprising of graphene quantum capacitance C_{qG}, insulator capacitance C_I of bilayer hBN and quantum capacitance of MoS_2 C_{qM}. **c** Showcase of relevant band structure parameters used in the model development. Here E_F is the Fermi level; E_{CG}, E_{VG}, E_{CM}, E_{VM}, respectively denotes conduction band minima and valence band maxima of graphene and MoS_2. **d** Comparison between analytical dispersion relations obtained from tight-binding Hamiltonian and DFT data. **e** Plot of non-linear relation between inversion charge density in MoS_2 (Q_I') and its surface potential Ψ_S. Non-linearity of the relation increases with decreasing d_1

case due to the trade-off between V_p reduction and C_{gg} increment. The higher capacitance value for $d_1 = 3.2$ Å drives the drain current of the transistor with $d_1 = 3.2$ Å to be greater than that with $d_1 = 3.4$ Å. On the other hand, upon introduction of n-type doping in MoS_2, the threshold voltage of the device decreases and accordingly I_{DC} attains a much higher value (~105 μA/μm) at saturation (see Supplementary Information). Conversely, the threshold voltage of the transistor with p-type MoS_2 as channel material increases and I_{DC} saturates with a value as small as ~17 μA/μm (see Supplementary Information). We also plot the nature of two important transcapacitances: C_{gd} (calculated at $V_{GS} = 1.5$ V) and C_{dg} (calculated at $V_{DS} = 1.5$ V) in Fig. 4(f), which follow the similar trends as that of C_{gg}. For all these characteristics, the mobility value is taken to be 400 cm^2/Vs as estimated by the DFT + Bolzmann formalism.[36]

Digital logic performance

The equations for proposed compact device model are shown in Fig. 5 (where V_{CB} is channel potential/imref; W and L—both taken to be 1 μm, specifies the channel width and length respectively; μ and D, respectively denotes low-field mobility and field-dependent diffusivity; Q_G, Q_D, Q_S and i_G, i_D, i_S refers to terminal charges and currents at gate, drain and source respectively; and finally Q'_{I_n} and ψ_{S_n} symbolizes the values of Q_I' and Ψ_S at nth breakpoint). The surface potential equation $\zeta = 0$ (Eqn. (F1) in Fig. 5) is a function of gate bias, imref and material parameters, which are obtained from the DFT calculations. We solve this equation numerically for different bias conditions to calculate the surface potentials and inversion charge densities, and thereby the dc drain current (I_{DC}) and terminal charges (Q_G, Q_D, and Q_S) become explicit polynomials of them. Efficient algorithms[45,46] could be developed in this regard to solve such equations inside the circuit simulator. We implement this model in professional circuit simulator[34] or SPICE (simulation program for integrated circuit emphasis) using its Verilog–AMS interface in order to conduct static and transient simulation of integrated circuits. As shown in Fig. 5, SPICE engine assigns terminal voltages (viz. V_G, V_D and V_S) to the Verilog-AMS module, which computes terminal currents (viz. i_G, i_D and i_S) according to Eqn. (F1)–(F5), and then returns them to the individual terminals to be further processed by the SPICE engine. A direct implementation of these equations in SPICE without any numerical pitfall is very tedious and time-consuming process. For simulation of basic logic circuits, however, a look-up table approach will suffice and be followed in this work. First, we have designed a resistive-load inverter (see Fig. 6(a)) and simulated its voltage transfer characteristics (VTC) with the input voltage varying from 0 V to 1.5 V, as plotted in Fig. 6(b). It reflects the effect of bandgap broadening of graphene by indicating the positive shift of threshold voltage of the inverter, designed with the MISFET having smaller d_1. Also plotted in Fig. 6(b) are the VTC of the logic inverters designed with the MISFETs having n and p-type MoS_2 monolayers as semiconducting channel materials. As depicted in Fig. 6(b), the inverter corresponding to n-type MoS_2 channel experiences a smaller threshold voltage, whereas the inverter with p-type MoS_2 has a greater threshold voltage. Clearly, this effect of threshold voltage modification is quite similar to the effect of band gap modulation of graphene. Subsequently, we have designed 15-stage ring oscillator circuits with these resistive-load inverters to study the transient response. The output voltage waveforms of three ring oscillators (each designed with the MISFETs with different values of d_1) are shown in Fig. 6(c). It exhibits moderate changes in oscillation frequencies as mentioned in the figure itself. To be precise, variation of d_1 by ± 0.2 Å results in increment of the oscillating frequency by a factor of

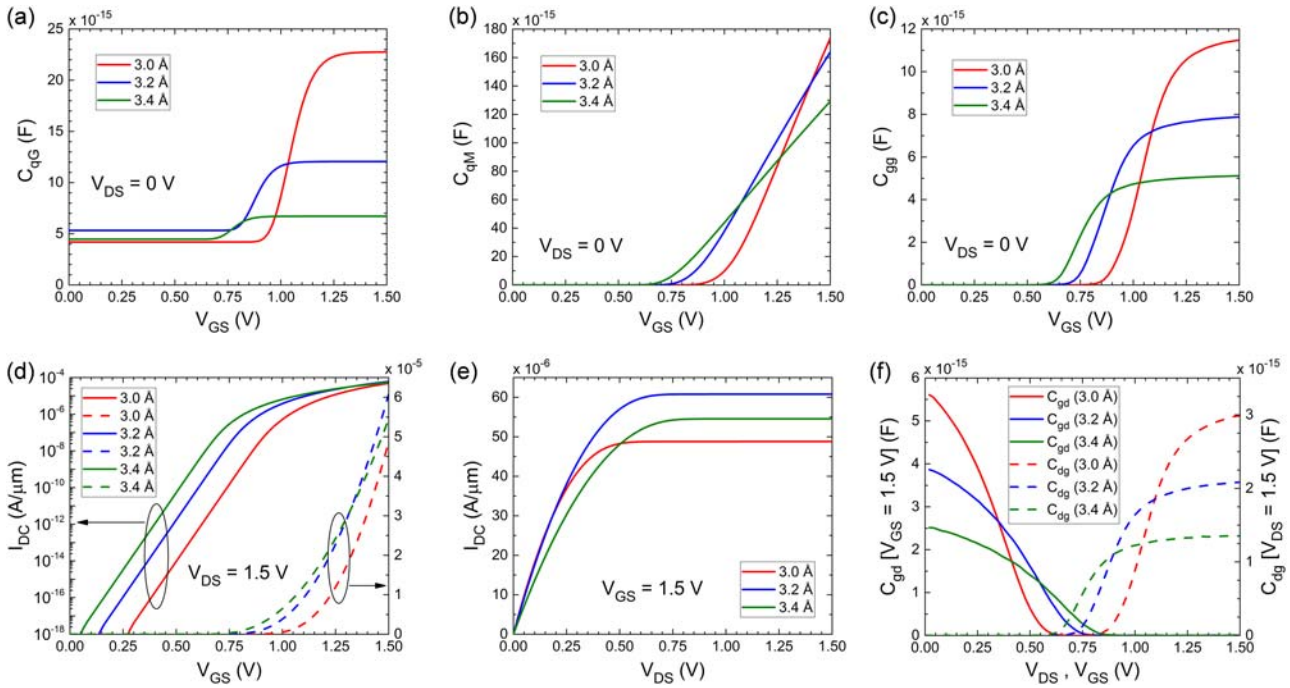

Fig. 4 Plot of **a** C_{qG}, **b** C_{qM}, and **c** C_{gg} with respect to gate-to-source voltage V_{GS} (keeping drain-to-source voltage $V_{DS} = 0$ V) for different values of d_1. In **a** and **b**, both C_{qG} and C_{qM} are confined within the quantum capacitance limit. In **c**, C_{gg} is mostly dominated by C_{qG}. **d** and **e**, respectively depicts the transfer and drain characteristics of the vdWH-based MISFET. **f** Plot of the transcapacitances C_{gd} (with respect to V_{DS}, keeping $V_{GS} = 1.5$ V) and C_{dg} (with respect to V_{GS}, keeping $V_{DS} = 1.5$ V). For **c** and **f**, all the terminal capacitances are calculated as $C_{XY} = \partial Q_X / \partial V_Y$, where X and Y are the terminals of the device

1.085 and conversely, a decrement of the same by a factor of 0.85. The ring oscillator featuring $d_1 = 3.0$ Å possesses the lowest frequency of oscillation among all. The waveforms of the oscillators featuring MISFETs with n and p-type MoS_2 channel have also been plotted in Fig. 6(c) and similar trends of increment and decrement of oscillating frequencies are observed. For n-type doping, the frequency increases to $1.125f_0$ and it decreases to $0.85f_0$ for p-type doping, with $f_0 = 5.75$ MHz being the frequency of the ring oscillator featuring undoped MoS_2 channel and $d_1 =$ 3.2 Å. Good convergence of the simulations in all cases advocates the practicality and applicability of the proposed model for large-scale circuit simulation in order to assess the device performance at circuit level at the early stage of technology development.

DISCUSSION

In this article, we propose a first principle-based 'atom-to-circuit' modeling methodology, which can assess the impact and predict the performance of a material or material-system at device and circuit level even in the absence of any experimental data. We demonstrate two applications of the proposed model: (i) effect of band-gap fluctuation of graphene on the circuit performance and (ii) material-device-circuit co-assessment scheme considering semiconductor doping as a design parameter. A schematic view as depicted in Fig. 6(d) captures the basic philosophy of the proposed modeling scheme, which bridges between first principle-based material modeling tools and industry standard circuit simulators. The model equations could further be simplified to be applicable for any 2D-material-channel MOSFET with conventional gate stack. Furthermore, since we use industry-standard DD formalism for SPICE model development, the proposed model is 'core' in nature and standard techniques (i.e., pre-correction) for including several small geometry effects (such as drain induced barrier lowering, velocity saturation etc.) could easily be conjoined with it. Henceforth, this stupendous flexibility and extensive scope of applicability should encourage our modeling framework to stand high.

METHODS

Atomistic model development

In order to carry out the first principles-based calculations, the DFT code as implemented in atomistix tool kit (ATK)[30] is employed in conjunction with generalized gradient approximation (GGA) exchange correlation and the Perdew-Burke-Ernzerhof (PBE) functional.[47] Apart from that, we have used the OpenMX (Open Source package for Material eXplorer) norm-conserving pseudopotentials[48,49] as implemented in ATK database with pseudo-atomic orbitals (PAO) and 'medium' basis sets for the constituent atoms. To be precise, the LCAO (linear combination of atomic orbitals) basis sets for 'C', 'B', 'N' and 'S' atoms are adopted to be $s^2p^2d^1$, and $s^3p^2d^1$ for 'Mo' atom. The k-points in the Monkhorst-Pack grid[50] were set to $9 \times 9 \times 1$ along with the density mesh cutoff of 90 Hartree. The maximum iteration steps were set to 200 using Pulay mixer algorithm and the Poisson solver we followed was the fast Fourier transform (FFT). To account for the vdW interactions in the heterostructures, we have incorporated Grimme DFT-D2 semi-empirical correction[51] as defined in ATK database in combination with counterpoise correction[52] that deals with the basis set superposition error (BSSE) of LCAO basis sets. Furthermore, for all the structures, we have provided sufficient vacuum in the perpendicular, i.e., normal-to-the-plane direction to avoid spurious interactions between periodic images. The geometry optimization of the unit cells of graphene, hBN, and semiconducting 2H-MoS_2 were performed using the LBFGS (Limited-memory Broyden-Fletcher-Goldfarb-Shanno) algorithm[53] with maximum stress tolerance value of 0.001 eV/Å^3 and force tolerance of 0.01 eV/Å. Keeping in mind the commensurability condition, the interfaces between these constituent materials were formed by 4×4 MoS_2 supercell (lattice parameter = 12.77 Å), 5×5 hBN supercell (lattice parameter = 12.63 Å) and 5×5 graphene supercell (lattice parameter = 12.36 Å), leaving 0.75% and 1.88% mean absolute strain on hBN and graphene respectively, which are reasonably small. In order to model n and p-type doped MoS_2 monolayers, we have exercised the method of electrostatic doping (using n and p-type atomic compensation charges[54,55]) available in ATK[30] instead of explicitly substituting the Mo atoms by elemental dopant atoms (e.g., Nb for p-type[56] and Au, Re for n-type[57]). This is because in order to achieve

$$\zeta\left(V_{GS},V_{CB},\Delta_{GC},\Delta_{GV},\Delta_{MC},\Delta_{MV},m^*_{eG},m^*_{hG},m^*_{eM},m^*_{hM},\psi_S\right)=0 \quad \text{(F1)}$$

$$I_{DC}=\frac{W}{L}\sum_{n=1}^{3}\left\{-\frac{\mu}{2}\left(\psi_{S_n}-\psi_{S_{n-1}}\right)\left(Q'_{I_n}+Q'_{I_{n-1}}\right)+D\left(Q'_{I_n}-Q'_{I_{n-1}}\right)\right\} \quad \text{(F2)}$$

$$Q_G=-WL\frac{\sum_{n=1}^{3}\left\{-\frac{\mu}{3}\left(\psi_{S_n}-\psi_{S_{n-1}}\right)\left(Q'^{\,2}_{I_n}+Q'^{\,2}_{I_{n-1}}+Q'_{I_n}Q'_{I_{n-1}}\right)+\frac{D}{2}\left(Q'^{\,2}_{I_n}-Q'^{\,2}_{I_{n-1}}\right)\right\}}{\sum_{n=1}^{3}\left\{-\frac{\mu}{2}\left(\psi_{S_n}-\psi_{S_{n-1}}\right)\left(Q'_{I_n}+Q'_{I_{n-1}}\right)+D\left(Q'_{I_n}-Q'_{I_{n-1}}\right)\right\}} \quad \text{(F3)}$$

$$Q_D=WL\frac{\left[\sum_{n=1}^{3}\{\eta_n\}+\sum_{n=1,2}^{n<p\le 3}\{\eta_{n,p}\}\right]}{\left[\sum_{n=1}^{3}\left\{-\frac{\mu}{2}\left(\psi_{S_n}-\psi_{S_{n-1}}\right)\left(Q'_{I_n}+Q'_{I_{n-1}}\right)+D\left(Q'_{I_n}-Q'_{I_{n-1}}\right)\right\}\right]^2} \quad \text{(F4)}$$

$$Q_S=-\left(Q_G+Q_D\right) \quad \text{(F5)}$$

$$\eta_n=D^2\left\{\frac{1}{3}\left(Q'^{\,3}_{I_n}-Q'^{\,3}_{I_{n-1}}\right)-\frac{Q'_{I0}}{2}\left(Q'^{\,2}_{I_n}-Q'^{\,2}_{I_{n-1}}\right)\right\}+\frac{\mu^2}{10}\left(\psi_{S_n}-\psi_{S_{n-1}}\right)^2\left\{Q'^{\,3}_{I_n}+\frac{2}{3}Q'^{\,3}_{I_{n-1}}+2Q'_{I_n}Q'_{I_{n-1}}\left(Q'_{I_n}+\frac{2}{3}Q'_{I_{n-1}}\right)\right\}+\frac{D\mu}{24}\left(\psi_{S_n}-\psi_{S_{n-1}}\right)\left\{8Q'_{I0}\left(Q'^{\,2}_{I_n}+Q'^{\,2}_{I_{n-1}}+Q'_{I_n}Q'_{I_{n-1}}\right)-3\left(Q'^{\,3}_{I_{n-1}}+3Q'^{\,3}_{I_n}+Q'_{I_n}Q'_{I_{n-1}}\left(3Q'_{I_n}+Q'_{I_{n-1}}\right)\right)\right\}$$

$$\eta_{n,p}=\left\{-\frac{\mu}{2}\left(\psi_{S_n}-\psi_{S_{n-1}}\right)\left(Q'_{I_n}+Q'_{I_{n-1}}\right)\right\}\times\left\{\frac{D}{2}\left(Q'^{\,2}_{I_p}-Q'^{\,2}_{I_{p-1}}\right)-\frac{\mu}{3}\left(\psi_{S_p}-\psi_{S_{p-1}}\right)\left(Q'^{\,2}_{I_p}+Q'^{\,2}_{I_{p-1}}+Q'_{I_p}Q'_{I_{p-1}}\right)\right\}$$

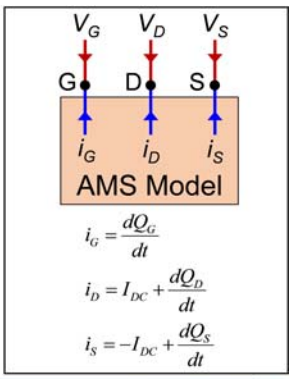

Fig. 5 Equations (F1)–(F5) are mathematical expressions for the proposed compact device model. The closed form expressions of dc drain current I_{DC} and terminal charges viz. Q_G, Q_D, Q_S are obtained employing piecewise charge linearization technique. Inset: SPICE engine assigns terminal voltages (viz. V_G, V_D, and V_S) to the Verilog-AMS module, which computes terminal currents (viz. i_G, i_D, and i_S) according to Eqn. (F1)–(F5), and then returns them to the individual terminals to be processed by the SPICE engine

a practical n or p-type doping concentration in MoS_2 (typically $1\times10^{17}-1\times10^{19}$ cm^{-3})[58] by substitutional doping, a very large supercell is needed, which demands very large computation cluster. Such electrostatic doping scheme is very effective and advantageous since it does not depend on exact detail of dopant atoms.[54] Here, the doping concentration is set to 1×10^{19} cm^{-3} for both n and p-type doping.

Development of energy dispersion relations

We start with the 2-band Hamiltonian of graphene that incorporates the effect of sublattice symmetry breaking.[42,59,60] In nearest-neighbor π–electron tight-binding parlance, where sublattice symmetry breaking can be parameterized by a mass term, the Hamiltonian describing electronic properties of graphene near the Fermi level can be approximated as[59]:

$$H=\begin{pmatrix}\Delta & \hbar v_F\left(k_x-ik_y\right)\\ \hbar v_F\left(k_x+ik_y\right) & -\Delta\end{pmatrix} \quad (1)$$

where, k is wave vector relative to Dirac (K or K′) point, $\hbar$ is modified Planck's constant and Δ is the onsite energy difference between two sublattices A and B, which in turn equals to $m^*v_F^2$ ($m^*=m^*_{eG}$ or m^*_{hG}). This Hamiltonian operates on spinors $\Psi=\begin{pmatrix}\Phi_A\\ \Phi_B\end{pmatrix}$ (where Φ_A and Φ_B are the amplitudes of the wavefunctions of two sublattices), to produce the energy eigenvalues of the form: $E=\pm\sqrt{\Delta^2+(\hbar v_F k)^2}$. For graphene on top of hBN, $\Delta\neq0$ and the energy dispersions near the Dirac points can be approximated to be parabolic having the form[28]:

$$E(k)\approx\pm\left[\Delta+\frac{(\hbar v_F k)^2}{2\Delta}\right] \quad (2)$$

Here, '±' sign corresponds to the conduction band (CB) with $\Delta=\Delta_{GC}$ and valence band (VB) with $\Delta=\Delta_{GV}$ respectively, defining the non-zero bandgap introduced at Dirac point as: $E_{gG}=\Delta_{GC}+\Delta_{GV}$. Although for ±0.2 Å variation of d_1, the bandgap opening is symmetric (i.e., $\Delta_{GC}=\Delta_{GV}$) about E_F, in general Δ_{GC} may not be equal to Δ_{GV} for further reduction of d_1. On the other hand, the band structure of MoS_2 can also be approximated to be simple parabolic in nature, written as[23,25]:

$$E(k)=\pm\left(\Delta_{MC(MV)}+\frac{\hbar^2k^2}{2m^*_{eM(hM)}}\right) \quad (3)$$

for CB (VB) (where '+': CB and '–': VB), featuring a bandgap of $E_{gM}=\Delta_{MC}+\Delta_{MV}$.

Thereafter, we obtain the expressions for density of states (DOS) of conduction and valence bands of graphene and MoS_2 as: $g_{Gn}=\frac{g_{sG}g_{vG}\Delta_{GC}}{2\pi(\hbar v_F)^2}$ (for graphene CB), $g_{Gp}=\frac{g_{sG}g_{vG}\Delta_{GV}}{2\pi(\hbar v_F)^2}$ (for graphene VB), $g_{Mn}=\frac{g_{sM}g_{vM}m^*_{eM}}{2\pi\hbar^2}$ (for MoS_2 CB) and $g_{Mp}=\frac{g_{sM}g_{vM}m^*_{hM}}{2\pi\hbar^2}$ (for MoS_2 VB). Here, g_{sG}, g_{sM} are spin degeneracies (both taken as 2) and g_{vG}, g_{vM} are valley degeneracies (both taken as 2) of graphene and MoS_2 respectively.

MIS capacitor modeling

Employing Fermi-Dirac statistics, we first calculate the intrinsic carrier concentrations in graphene (MoS_2) as:

$$n_{G(M)}=g_{Gn(Mn)}KT\ln\left[1+\exp\left(-\frac{\Delta_{GC(MC)}}{KT}\right)\right] \quad (4a)$$

$$p_{G(M)}=g_{Gp(Mp)}KT\ln\left[1+\exp\left(-\frac{\Delta_{GV(MV)}}{KT}\right)\right] \quad (4b)$$

where, n_G (n_M) and p_G (p_M) stands for electron and hole concentrations in graphene and MoS_2 respectively, K is the Boltzman constant and T is temperature (taken as 300 K). Now, if we symbolize net electron and hole concentrations in graphene and MoS_2 (upon application of V_G) by n_{netG}, p_{netG}, n_{netM} and p_{netM} respectively, then the total charge densities in these two layers can be written as $Q'_G=q(p_{netG}-n_{netG})$ for graphene and $Q'_I=q(p_{netM}-n_{netM})$ for MoS_2, where

$$n_{netG(netM)}=g_{Gn(Mn)}KT\ln\left[1+\exp\left(-\frac{\Delta_{GC(MC)}}{KT}\mp\frac{q\Psi_{G(S)}}{KT}\right)\right] \quad (5a)$$

$$p_{netG(netM)}=g_{Gp(Mp)}KT\ln\left[1+\exp\left(-\frac{\Delta_{GV(MV)}}{KT}\pm\frac{q\Psi_{G(S)}}{KT}\right)\right] \quad (5b)$$

Here, we consider the charge distribution inside MoS_2 to be an ideal 2D sheet having no spatial variation, which removes the burden of solving Poisson's equation beforehand. On the other side, Ψ_G, Ψ_I and Ψ_S sum up to satisfy the potential balance equation, which is:

$$V_G=\Psi_G+\Psi_I+\Psi_S \quad (6)$$

where Ψ_I can be calculated as:

$$\Psi_I=Q'_G/C_I=-Q'_I/C_I \quad (7)$$

Here, we neglect any leakage current through the hBN layers. Now using Eqns (5)–(7), the charge balance equation can be solved numerically for Ψ_S,

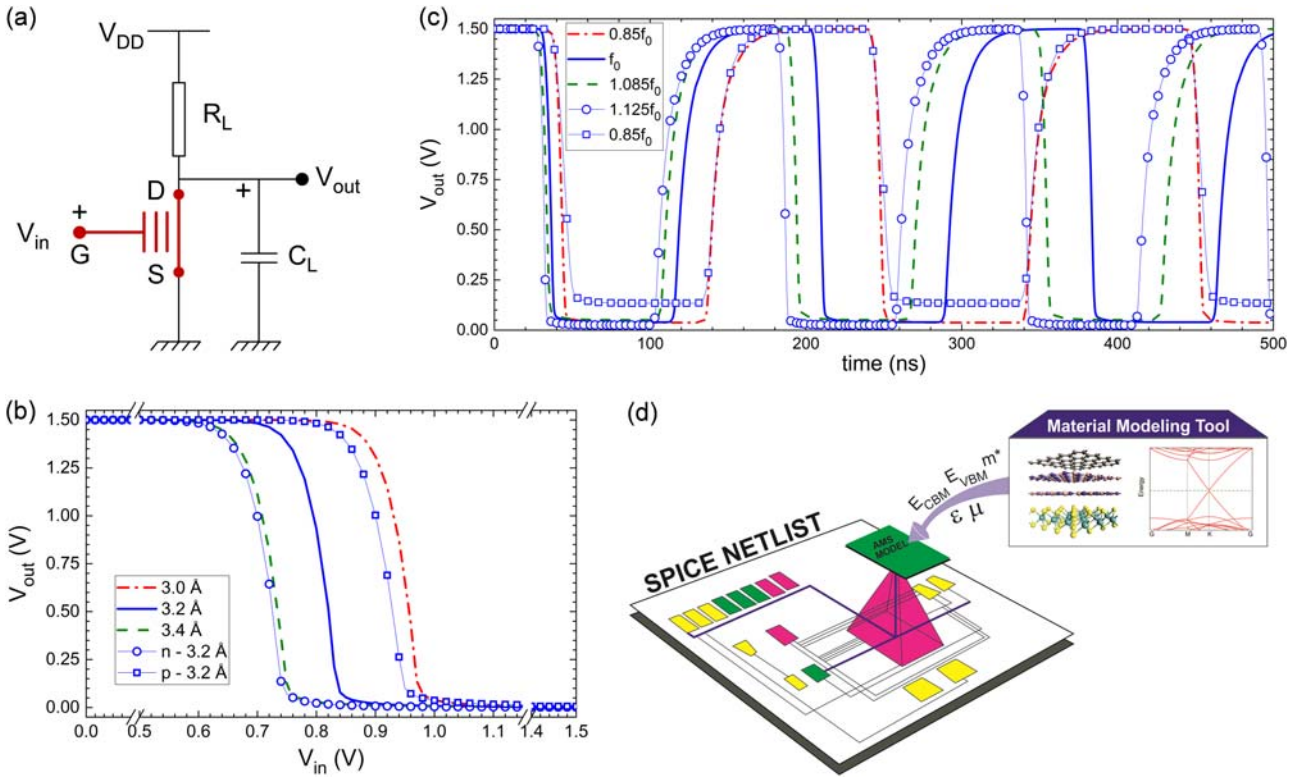

Fig. 6 **a** Circuit diagram for a resistive load inverter, designed using the graphene-hBN-hBN-MoS_2 vdWH based MISFET. R_L is the load resistor and C_L is external capacitive load at output. **b** DC transfer characteristics of the logic inverter, indicating a positive shift of the threshold voltage of the inverter circuit with decreasing d_1. It also depicts the DC characteristics of the inverters designed with MISFETs featuring n and p-doped MoS_2 monolayers. For n-type doping the threshold voltage decreases, whereas the opposite happens for p-type doping. **c** Output frequency waveform of a 15-stage ring oscillator, designed with these inverters. It shows the change in output frequency as a result of varying d_1 from its equilibrium value and also as a result of doping in MoS_2. Here f_0=5.75 MHz. The legend convention is same as that of **b**. **d** A schematic view of the basic philosophy behind the proposed model which reveals that, the model (i.e. AMS module) works as a bridge between first principles-based material modeling tools and industry standard circuit simulators

which can be written as:

$$Q'_G + Q'_I = 0 \tag{8}$$

that ultimately takes the form of Eqn. (F1) of Fig. 5 with V_{CB} set to zero.

Once we get the numeric values of Ψ_S, the other two potentials Ψ_G and Ψ_I can be easily computed, thereby facilitating the computation of quantum capacitances viz. C_{qG} and C_{qM} using the following expressions:

$$C_{qG} = q^2 \frac{g_{sG} g_{vG}}{2\pi(\hbar v_F)^2} \times \left\{ \begin{array}{l} \Delta_{GC}\left[1+\exp\left(\frac{\Delta_{GC}+q\Psi_G}{KT}\right)\right]^{-1} \\ +\Delta_{GV}\left[1+\exp\left(\frac{\Delta_{GV}-q\Psi_G}{KT}\right)\right]^{-1} \end{array} \right\} \tag{9a}$$

$$C_{qM} = q^2 \frac{g_{sM} g_{vM}}{2\pi\hbar^2} \times \left\{ \begin{array}{l} m^*_{eM}\left[1+\exp\left(\frac{\Delta_{MC}-q\Psi_S}{KT}\right)\right]^{-1} \\ +m^*_{hM}\left[1+\exp\left(\frac{\Delta_{MV}+q\Psi_S}{KT}\right)\right]^{-1} \end{array} \right\} \tag{9b}$$

For a similar device with more than two hBN layers, the model equations will remain all the same, however, the parameters viz. Δ_{GC}, Δ_{GV}, Δ_{MC}, Δ_{MV}, v_F, m^*_{eM}, m^*_{hM} and ε need to be recalculated using DFT. Similarly, for the heterostructures with n or p-type MoS_2 monolayers, the whole set of equations will essentially remain same, provided the aforesaid parameters are obtained from DFT calculations of that particular heterostructure. This is because the effect of doping has been effectively captured here through the positions of the band extrema in the energy scale and corresponding effective masses and that basically rules out the necessity of introducing a doping term explicitly in the charge neutrality equation. It is noteworthy that the band structure obtained from DFT calculation is qualitatively similar to the previously reported work,[18] which uses different simulation toolkit and deals with single hBN layer. In this aspect, the proposed model equations are independent of the exchange-correlation functionals or pseudopotentials; only the relevant model parameters need to be calculated accordingly.

MISFET modeling

To formulate the drain current and terminal charges, we adopt the semiclassical DD formalism,[26,61] which has been practiced in industrial top–down compact modeling methodology over the years. We can take the benefits arising from well-established techniques available to add different small geometry effects to the core model as future work. It also allows us to develop the model without using any unphysical model parameters or interpolating function. Since the proposed model involves only material parameters (CBMs, VBMs, effective masses, dielectric constant, and mobility), which could be calculated by first principles-based methods, it can predict the device and circuit characteristics just from the crystallographic information of the constituent materials.

In DD formalism, the dc drain current equation reads[61]:

$$I_{DC} = \frac{W}{L}\left[\mu \int_{\Psi_{S0}}^{\Psi_{SL}} \left(-Q'_I\right) d\Psi_S + D \int_{Q'_{I0}}^{Q'_{IL}} dQ'_I\right] \tag{10}$$

where, Ψ_{S0}, Ψ_{SL} and Q'_{I0}, Q'_{IL} are the values of Ψ_S and Q'_I at source ($x = 0$) and drain ($x = L$) end of the transistor respectively, with x being considered as the direction of transport. Since we explicitly use FD statistics to describe carrier occupation probability, instead of using typical Einstein relation, we treat the diffusivity coefficient D to be bias dependent.[62] We express D as[63] $D = \mu Q'_I \left(d\Psi_S/dQ'_I\right)\big|_{V_{DS}=0}$ to ensure zero drain current at $V_{DS} = 0$. Due to complex nature of ζ, an analytical solution of Eq. (9) is not possible. Hence, we apply charge linearization technique[27] to obtain a closed form expression of the drain current. In case of conventional Si-MOSFET, for a given bias condition, Q'_I changes quasi-linearly with Ψ_S along the channel and hence Q'_I is approximated as a linear function of Ψ_S in Eqn. (10), which results in a quadratic relationship between I_{DC} and Ψ_S. Such relationship is very useful to obtain closed form expression of terminal charges under Ward-Dutton (WD)[64] charge partitioning scheme. However, as shown in Fig. 3(e), due to the band-gap opening in graphene, Q'_I does

not always maintain a linear relationship with Ψ_S in case of vdWH MISFET. Thus, in this work we adopt PWCL technique[27] (see Supplementary Information). Using the expression of drain current, the terminal charges could be computed under WD charge partitioning[64] scheme as: $Q_G = -W\int_0^L Q'_{lx}(x)dx$, $Q_D = W\int_0^L \frac{x}{L}Q'_{lx}(x)dx$ and $Q_S = -(Q_G + Q_D)$, where Q'_{lx} is the value of Q'_l at any position x in the channel. Similar to state-of-the-art surface potential-based Si-MOSFET models,[65] Eqns. (F2)–(F5) are 'single-piece-continuous' equations, valid for all regimes of transistor operation.

Data availability

The authors declare that the main data supporting the findings of this study are available within the paper and its Supplementary Information file. MATLAB and Verilog-AMS codes are freely available at osf.io/me236. Other relevant data are available from the corresponding author upon request.

ACKNOWLEDGEMENTS

This work was supported by Science and Engineering Research Board (SERB), Department of Science and Technology (DST), Government of India, under Grant SB/S3/EECE/0209/2015. We would like to thank G.N. Kadloor, DESE-IISc, for his help in preparing Fig. 6(d).

AUTHOR CONTRIBUTIONS

B.D. performed the DFT calculations, developed the compact device model, conducted SPICE simulations, and analyzed final results. S.M. conceived the problem statement and overall supervised the work. All authors contributed in the writing.

ADDITIONAL INFORMATION

Supplementary information accompanies the paper on the *npj 2D Materials and Applications* website (https://doi.org/10.1038/s41699-018-0073-3).

Competing interests: The authors declare no competing interests.

Publisher's note: Springer Nature remains neutral with regard to jurisdictional claims in published maps and institutional affiliations.

REFERENCES

1. Shih, C-J. et al. Tuning on-off current ratio and field-effect mobility in a MoS_2-graphene heterostructure via Schottky barrier modulation. *ACS Nano* **8**, 5790–5798 (2014).
2. Deng, Y. et al. Black Phosphorus-monolayer MoS_2 van der Waals heterojunction p–n diode. *ACS Nano* **8**, 8292–8299 (2014).
3. Lee, G. -H. et al. Highly stable, dual-gated MoS_2 transistors encapsulated by hexagonal boron nitride with gate-controllable contact, resistance, and threshold voltage. *ACS Nano* **9**, 7019–7026 (2015).
4. Ling, X. et al. Parallel stitching of 2D materials. *Adv. Mater.* **28**, 2322–2329 (2016).
5. Pant, A. et al. Fundamentals of lateral and vertical heterojunctions of atomically thin materials. *Nanoscale* **8**, 3870–3887 (2016).
6. Geim, A. K. & Grigorieva, I. V. Van der Waals heterostructures. *Nature* **499**, 419–425 (2013).
7. Ma, Z. et al. Tunable band structures of heterostructured bilayers with transition–metal dichalcogenide and MXene monolayer. *J. Phys. Chem. C.* **118**, 5593–5599 (2014).
8. Roy, T. et al. Dual–gated MoS_2/WSe_2 van der Waals tunnel diodes and transistors. *ACS Nano* **9**, 2071–2079 (2015).
9. Roy, T. et al. Field-effect transistors built from all two-dimensional material components. *ACS Nano* **8**, 6259–6264 (2014).
10. Lee, G. -H. et al. Flexible and transparent MoS_2 field–effect transistors on hexagonal boron nitride–graphene heterostructures. *ACS Nano* **7**, 7931–7936 (2013).
11. Cheng, R. et al. Multifunctional tunneling devices based on graphene/h-BN/$MoSe_2$ van der Waals heterostructures. *Appl. Phys. Lett.* **110**, 173507 (2017).
12. Jeong, H. et al. Metal-insulator-semiconductor diode consisting of two-dimensional nanomaterials. *Nano Lett.* **16**, 1858–1862 (2016).
13. Zhang, K. et al. Interlayer transition and infrared photodetection in atomically thin type-II $MoTe_2$/MoS_2 van der Waals heterostructures. *ACS Nano* **10**, 3852–3858 (2016).
14. Withers, F. et al. Light-emitting diodes by band-structure engineering in van der Waals heterostructures. *Nat. Mater.* **14**, 301–306 (2015).
15. Ross, J. S. et al. Electrically tunable excitonic light-emitting diodes based on monolayer WSe_2 p-n junctions. *Nat. Nanotechnol.* **9**, 268–272 (2014).
16. Furchi, M. M., Pospischil, A., Libisch, F., Burgdörfer, J. & Mueller, T. Photovoltaic effect in an electrically tunable van der Waals heterojunction. *Nano Lett.* **14**, 4785–4791 (2014).
17. Vu, Q. A. et al. Tuning carrier tunneling in van der Waals heterostructures for ultrahigh detectivity. *Nano Lett.* **17**, 453–459 (2017).
18. Zan, W., Geng, W., Liu, H. & Yao, X. Electric-field and strain-tunable electronic properties of MoS_2/h-BN/graphene vertical heterostructures. *Phys. Chem. Chem. Phys.* **18**, 3159–3164 (2016).
19. Mounet, N. et al. Two-dimensional materials from high-throughput computational exfoliation of experimentally known compounds. *Nat. Nanotechnol.* **13**, 246–252 (2018).
20. Tung, R. T. Formation of an electric dipole at metal-semiconductor interfaces. *Phys. Rev. B* **64**, 205310 (2001).
21. Yakovkin, I. N. Dirac cones in graphene, interlayer interaction in layered materials, and the band gap in MoS_2. *Crystals* **6**, 143 (2016).
22. Gong, C., Colombo, L., Wallace, R. M. & Cho, K. The unusual mechanism of partial Fermi level pinning at metal-MoS_2 interfaces. *Nano Lett.* **14**, 1714–1720 (2014).
23. Cao, W., Kang, J., Liu, W. & Banerjee, K. A compact current-voltage model for 2D semiconductor based field-effect transistors considering interface traps, mobility degradation, and inefficient doping effect. *IEEE Trans. Electron Devices* **61**, 4282–4290 (2014).
24. Marin, E. G., Bader, S. J. & Jena, D. A new holistic model of 2-D semiconductor FETs. *IEEE Trans. Electron Devices* **65**, 1239–1245 (2018).
25. Yadav, C., Agarwal, A. & Chauhan, Y. S. Compact modeling of transition metal dichalcogenide based thin body transistors and circuit validation. *IEEE Trans. Electron Devices* **64**, 1322–1329 (2017).
26. Zebrev, G. I. & Useinov, R. G. Simple model of current-voltage characteristics of a metal–insulator–semiconductor transistor. *Fiz. Tekhn. Polupr. (Sov. Phys. Semicond.)* **24**, 777–781 (1990).
27. Jandhyala, S., Abraham, A., Anghel, C. & Mahapatra, S. Piecewise linearization technique for compact charge modeling of independent DG MOSFET. *IEEE Trans. Electron Devices* **59**, 1974–1979 (2012).
28. Fan, Y., Zhao, M., Wang, Z., Zhang, X. & Zhang, H. Tunable electronic structures of graphene/boron nitride heterobilayers. *Appl. Phys. Lett.* **98**, 083103 (2011).
29. *2D Semiconductors*. URL: http://www.2dsemiconductors.com/n-type-mos2/.
30. *QuantumWise Atomistix ToolKit* (*ATK*) *with Virtual NanoLab*, Synopsys Denmark, URL: http://quantumwise.com/. Last accessed: 18 Mar 2018.
31. *Vienna Ab initio Simulation Package* (*VASP*), Computational Materials Physics Sensengasse, Austria, URL: https://www.vasp.at/.
32. *CAmbridge Serial Total Energy Package* (*CASTEP*), Dassault Systèmes BIOVIA, URL: http://www.castep.org/.
33. *Eldo, Mentor Graphics.* URL: https://www.mentor.com/.
34. *SmartSpice, Analog Circuit Simulator–Users' Manual*, version 4.10.6.R (Silvaco Inc., Santa Clara, CA, 2014). URL: https://www.silvaco.com/.
35. Kumar, P., Chauhan, Y. S., Agarwal, A. & Bhowmick, S. Thickness and stacking dependent polarizability and dielectric constant of graphene-hexagonal boron nitride composite stacks. *J. Phys. Chem. C.* **120**, 17620–17626 (2016).
36. Gunst, T., Markussen, T., Stokbro, K. & Brandbyge, M. First-principles method for electron-phonon coupling and electron mobility: applications to two-dimensional materials. *Phys. Rev. B* **93**, 035414 (2016).
37. Wang, E. et al. Gaps induced by inversion symmetry breaking and second-generation Dirac cones in graphene/hexagonal boron nitride. *Nat. Phys.* **12**, 1111–1115 (2016).
38. Jung, J., DaSilva, A. M., MacDonald, A. H. & Adam, S. Origin of band gaps in graphene on hexagonal boron nitride. *Nat. Commun.* **6**, 6308 (2015).
39. Bokdam, M., Amlaki, T., Brocks, G. & Kelly, P. J. Band gaps in incommensurable graphene on hexagonal boron nitride. *Phys. Rev. B* **89**, 201404(R) (2014).
40. Skomski, R., Dowben, P. A., Driver, M. S. & Kelber, J. A. Sublattice-induced symmetry breaking and band-gap formation in graphene. *Mater. Horiz.* **1**, 563–571 (2014).
41. Kan, E. et al. Why the band gap of graphene is tunable on hexagonal boron nitride. *J. Phys. Chem. C.* **116**, 3142–3146 (2012).
42. Sławińska, J., Zasada, I. & Klusek, Z. Energy gap tuning in graphene on hexagonal boron nitride bilayer system. *Phys. Rev. B* **81**, 155433 (2010).
43. Komsa, H. -P. & Krasheninnikov, A. V. Electronic structures and optical properties of realistic transition metal dichalcogenide heterostructures from first principles. *Phys. Rev. B* **88**, 085318 (2013).
44. Kresse, G., Marsman, M., & Furthmüller, J. *VASP–The Guide, sec. 6.67.3 Finite Electric Fields* (2016). URL: http://cms.mpi.univie.ac.at/vasp/vasp.pdf.
45. Jandhyala, S. & Mahapatra, S. An efficient robust algorithm for the surface-potential calculation of independent DG MOSFET. *IEEE Trans. Electron Devices* **58**, 1663–1671 (2011).

46. Chen, T. L. & Gildenblat, G. Analytical approximation for the MOSFET surface potential. *Solid State Electron* **45**, 335–339 (2001).
47. Perdew, J. P., Burke, K. & Ernzerhof, M. Generalized gradient approximation made simple. *Phys. Rev. Lett.* **77**, 3865 (1996).
48. Ozaki, T. Variationally optimized atomic orbitals for large-scale electronic structures. *Phys. Rev. B* **67**, 155108 (2003).
49. Ozaki, T. & Kino, H. Numerical atomic basis orbitals from H to Kr. *Phys. Rev. B* **69**, 195113 (2004).
50. Monkhorst, H. J. & Pack, J. D. Special points for Brillouin-zone integrations. *Phys. Rev. B* **13**, 5188 (1976).
51. Grimme, S. Semiempirical GGA-type density functional constructed with a long-range dispersion correction. *J. Comput. Chem.* **27**, 1787–1799 (2006).
52. Boys, S. F. & Bernardi, F. The calculation of small molecular interactions by the differences of separate total energies. Some procedures with reduced errors. *Mol. Phys.* **19**, 553–566 (1970).
53. Liu, D. C. & Nocedal, J. On the limited memory BFGS method for large scale optimization. *Math. Program.* **45**, 503–528 (1989).
54. Stradi, D., Martinez, U., Blom, A., Brandbyge, M. & Stokbro, K. General atomistic approach for modeling metal semiconductor interfaces using density functional theory and nonequilibrium Green's function. *Phys. Rev. B. Condens. Matter* **93**, 155302 (2016).
55. Saha, D. & Mahapatra, S. Asymmetric junctions in metallic–semiconducting–metallic heterophase MoS_2. *IEEE Trans. Electron Devices* **64**, 2457–2460 (2017).
56. Suh, J. et al. Doping against the native propensity of MoS_2: Degenerate hole doping by cation substitution. *Nano Lett.* **14**, 6976–6982 (2014).
57. Park, H. -Y. et al. Wide-range controllable n-doping of molybdenum disulfide (MoS_2) through thermal and optical activation. *ACS Nano* **9**, 2368–2376 (2015).
58. Pham, V. P. & Yeom, G. Y. Recent advances in doping of molybdenum disulfide: Industrial applications and future prospects. *Adv. Mater.* **28**, 9024–9059 (2016).
59. Oostinga, J. B., Heersche, H. B., Liu, X., Morpurgo, A. F. & Vandersypen, L. M. K. Gate-induced insulating state in bilayer graphene devices. *Nat. Mater.* **7**, 151–157 (2008).
60. Hunt, B. et al. Massive Dirac fermions and Hofstadter butterfly in a van der Waals heterostructure. *Science* **340**, 1427–1430 (2013).
61. Tsividis, Y. & McAndrew, C. *Operation and Modeling of The MOS Transistor*, 3rd edn (Oxford University Press, New York, 2011).
62. Ghatak, K. P., Bhattacharya, S. & De, D. *Einstein Relation in Compound Semiconductors and Their Nanostructures*. (Springer, Berlin, Germany, 2009). Springer Series in Material Science.
63. Chakraborty, A. S. & Mahapatra, S. Compact model for low effective mass channel common double-gate MOSFET. *IEEE Trans. Electron Devices* **65**, 888–894 (2018).
64. Oh, S.-Y., Ward, D. & Dutton, R. Transient analysis of MOS transistors. *IEEE Trans. Electron Devices* **27**, 1571–1578 (1980).
65. Gildenblat, G. et al. PSP: An advanced surface-potential-based MOSFET Model for circuit simulation. *IEEE Trans. Electron Devices* **53**, 1979–1993 (2006).